Photoanodes with Fully Controllable Texture: The Enhanced Water Splitting Efficiency of Thin Hematite Films Exhibiting Solely (110) Crystal Orientation

Stepan Kment,*,† Patrik Schmuki,*,‡ Zdenek Hubicka,§ Libor Machala,† Robin Kirchgeorg,‡ Ning Liu,‡ Lei Wang,‡ Kiyoung Lee,‡ Jiri Olejnicek,§ Martin Cada,§ Ivan Gregora,§ and Radek Zboril*,†

†Regional Centre of Advanced Technologies and Materials, Joint Laboratory of Optics and Departments of Experimental Physics and Physical Chemistry, Faculty of Science, Palacky University, 17 listopadu 1192/12, 771 46 Olomouc, Czech Republic, ‡Department of Materials Science and Engineering, University of Erlangen-Nuremberg, Martensstrasse 7, D-91058 Erlangen, Germany, and §Institute of Physics, Academy of Sciences of the Czech Republic, Na Slovance 2, 14800 Prague, Czech Republic

ABSTRACT Hematite, α-Fe_2O_3, is considered as one of the most promising materials for sustainable hydrogen production *via* photoelectrochemical water splitting with a theoretical solar-to-hydrogen efficiency of 17%. However, the poor electrical conductivity of hematite is a substantial limitation reducing its efficiency in real experimental conditions. Despite of computing models suggesting that the electrical conductivity is extremely anisotropic, revealing up to 4 orders of magnitude higher electron transport with conduction along the (110) hematite crystal plane, synthetic approaches allowing the sole growth in that direction have not been reported yet. Here, we present a strategy for controlling the crystal orientation of very thin hematite films by adjusting energy of ion flux during advanced pulsed reactive magnetron sputtering technique. The texture and effect of the deposition mode on the film properties were monitored by XRD, conversion electron Mössbauer spectroscopy, XPS, SEM, AFM, PEC water splitting, IPCE, transient photocurrent measurements, and Mott–Schottky analysis. The precise control of the synthetic conditions allowed to fabricate hematite photoanodes exhibiting fully textured structures along (110) and (104) crystal planes with huge differences in photocurrents of 0.65 and 0.02 mA cm^{-2} (both at 1.55 V *versus* RHE), respectively. The photocurrent registered for fully textured (110) film is among record values reported for thin planar films. Moreover, the developed fine-tuning of crystal orientation having a huge impact on the photoefficiency would induce further improvement of thin hematite films mainly if cation doping will be combined with the controllable texture.

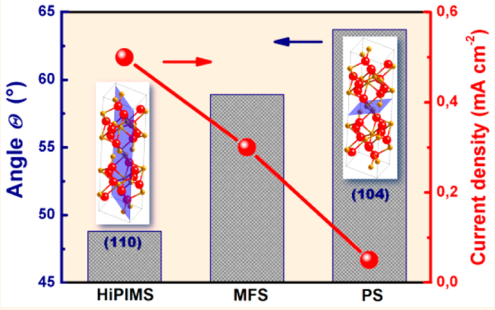

KEYWORDS: Hematite · iron oxide · texture · PEC water splitting · pulsed magnetron sputtering · conversion electron Mössbauer spectroscopy

Future needs for electric power generation driven by sustainable energy sources require a focused shift from fossil fuels to a combination of wind, water, solar and other renewable sources.[1] Hydrogen production from photoelectrochemical (PEC) water splitting driven by solar power is one such clean technology that can be used for environmentally friendly fuel production.[2] In a standard PEC cell, at least one of the electrodes comprises a photoactive material to simultaneously allow solar light harvesting and oxidation (taking place on a so-called photoanode) or reduction (on the photocathode) half reactions.[3] Iron oxide (α-Fe_2O_3) with hematite crystalline structure possesses many advantageous properties for use as a photoanode material.[4] The material's substantial light absorption, offering potential conversion of up to 17% of the sun's energy into hydrogen (band gap energy between 2.0 and 2.2 eV),[5] nontoxicity, high stability in aqueous environments, ample abundance and low cost are generally superior compared to other photoanodes. On the other hand, factors

* Address correspondence to stepan.kment@upol.cz (S. Kment), schmuki@ww.uni-enlangen.de (P. Schmuki), radek.zboril@upol.cz (R. Zboril).

Received for review March 22, 2015 and accepted June 17, 2015.

Published online June 17, 2015
10.1021/acsnano.5b01740

limiting high performance include its nonideal conduction band edge energy with respect to reductive hydrogen evolution, poor absorptivity, short charge diffusion length and large overpotential required to promote water oxidation. Several approaches have been used to address such nonideal optical and electronic behavior, *e.g.*, nanostructuring photoanodes,[6] application of a tandem cell approach,[7] and deposition of ultrathin isocrystalline films to passivate surface traps.[8,9]

Efficient transport of majority charge carriers through hematite is another key factor affecting the overall PEC performance of hematite. Substitutional doping increases the donor density, and thus carrier conductivity,[10] which is otherwise very poor. The earliest studies on the electrical properties of hematite were conducted by Morin.[11,12] Unusually, low values of basic electronic characteristics, including the mobility of charge carriers ($\sim 10^{-2}$ cm^2/(V s)), electrical conductivity ($\sim 10^{-14}$ Ω^{-1} cm^{-1}), conduction electron concentrations ($\sim 10^{18}$ cm^{-3} at 1000 K) and activation-energy type electron mobility ($\sim 10^{-2}$ cm^2 V^{-1} s^{-1}) were reported in these works. The electrical conductivity was shown to be related to Fe^{2+}/Fe^{3+} valence alternation on spatially localized iron (3d) orbitals, leading to electron transfer from one iron atom to another.[13] Later, computed modeling approaches reliably matched empirical data with a small polaron model that considered both the effect of the relatively large size of the Fe^{2+} ion and associated lattice distortion (polaron).[13−15] On the basis of this concept, the conductivity of electrons or holes is ascribed to hopping of polarons from site to site, which is conditional to a certain activation energy.[15,16] The temperature dependent activation energy, E_g, affects both the carrier generation and hopping mobility. The mobility of carriers has been shown to increase with increasing temperature, and therefore has been attributed to a phonon-assisted transport mechanism.[17] Pure hematite is ostensibly antiferromagnetic at room temperature (or weakly ferromagnetic owing to slight spin canting). The iron cations are in a high-spin d^5 configuration, in which the spins are coupled ferromagnetically along (001) basal planes and antiferromagnetically along the [001] direction, both assembled in so-called iron bilayers. Detailed investigations of hematite conductivity have revealed that, although the shortest Fe−Fe distance is along the [001] direction, the electrical conductivity is highly anisotropic, exhibiting up to 4 orders of magnitude higher electron transport with conduction along the iron bilayer (001) basal plane.[18] Interestingly, the perpendicular direction (parallel to [001]) was identified as the least facile transport pathway. This discrepancy was ascribed to the magnetic structure of hematite and explained on the basis of the Hund's rule. Specifically, electron transport (n-type conductivity) is allowed throughout the environment of parallel spins of the iron bilayers (along the same (001) plane), but it is forbidden to hop across the oxygen planes to an iron layer with opposite spins (moving along [001] direction). The only possible movement along the [001] direction is that of holes, defined as $Fe^{3+} \rightarrow Fe^{4+}$ electron transfer (p-type conductivity), which is slower than the movement of electrons in hematite.[17] Therefore, it is evident that methods to generate a specific and controllable texture may significantly improve the overall PEC activity of hematite photoanodes, as previously suggested by Grätzel *et al.*[19] However, this challenging aim has not yet been accomplished.

In the present work, we attempted to tune the crystal orientation and texture of hematite photoanodes by carefully controlling the energy of particles bombarding the substrate during a plasma assisted deposition procedure, *i.e.*, a magnetron sputtering process. Although the effect of deposition plasma parameters on the crystal structure of functional coatings has partially been discussed in several works,[20−22] none of them dealt with textured hematite photoanodes for PEC hydrogen production. The texture effect is generally associated with the surface chemistry, which influences the relative growth rates of the preferred crystal phases. The surface chemistry in sputtering based deposition processes is determined by the energy and nature (ionized or neutral metal species and ion-to-neutral flux ratio) of the impinging species.[23]

RESULTS AND DISCUSSION

The highly oriented hematite films examined in this study were fabricated by DC pulse reactive magnetron sputtering of a pure iron target working as a cathode in an Ar/O_2 gas mixture. Detailed description of the plasma deposition system and characterization techniques used is provided in Methods and Supporting Information Figure S1. Three different pulsing regimes of deposition magnetron discharge were used: (i) high impulse power magnetron sputtering mode (HiPIMS, 0.1 kHz), (ii) pulsing sputtering mode (PS, 1 kHz), and (iii) medium frequency sputtering mode (MFS, 50 kHz). As a result of different pulsing frequencies, f_P, and duty factors of a pulsing cycle, d_u, used, various cathode pulse current densities were reached. During each deposition, the average current, I_{AV}, and, consequently, average current density, j_{AV}, were kept constant at 600 mA and 32 mA/cm^2, respectively. The deposition plasma properties of each coating mode applied are summarized in Table 1. Except the X-ray powder diffraction (XRD) investigation, for which the hematite films were deposited onto amorphous fused silica and commercial $Pt/TiO_2/SiO_2/Si$ substrates, for all the remaining experiments presented, the hematite films were fabricated onto tin doped fluorine oxide substrates (FTO). After plasma coatings, all the

as-deposited films were thermally treated at the same temperature of 650 °C for 30 min in air to improve the crystallinity and charge transfer between hematite and charge collecting back contact (FTO) of the photoanode.

XRD patterns of films are presented in Figure 1 and Supporting Information Figure S2. It can be seen that the main variation was in the two most intense diffraction peaks corresponding to (110) and (104) reflections (in hexagonal coordinates) due to hematite, α-Fe_2O_3 (Figure 1). Only in the case of the MFS films, both these diffraction peaks occurred, suggesting the common polycrystalline hematite form. The main reflection observed in the spectrum for the PS film was from the (104) plane, whereas the desired preferential phase orientation along the (110) plane was unambiguously identified in the XRD pattern of the HiPIMS film. The (110) reflection peak broadening suggested that the HiPIMS films were composed of nanocrystalline grains when compared to the remaining types of tested photoanodes (MFS, PS).

Generally, the short duty cycles and low repetition frequency of the HiPIMS discharge (see Table 1) resulted in a high power density (~2 kW/cm^2) and high plasma density (~10^{18}–10^{19} m^{-3}) in the pulse; however, the values averaged over the whole period were much smaller (comparable or even lower than in the DC mode).[24] Owing to the high power of the HiPIMS pulse, a large fraction of the sputtered metal (here Fe) particles were ionized in the target region. Thus, the high energy ion flux, bombarding the substrate, was considerably enhanced, potentially hugely affecting the film crystallinity, texture, grain size, microstructure, density, adhesion, *etc.*, by influencing surface diffusion.[25] Surface diffusion is one of the most crucial parameters affecting the crystal growth. Energetic bombardment in the HiPIMS mode removes adsorbed impurities and facilitates surface diffusion and migration, allowing adatoms to be accommodated in certain preferential plane orientation,[26,27] in this study, orientation along the (110) plane. In comparison with the HiPIMS approach, the energy of particles impinging the substrate is negligible in the case of the MFS mode.[28] Thus, this mode resulted in formation of polycrystalline grains without any preferential plane orientations, which was consistent with XRD data of natural isotropic hematite powder (JCPDS 33-0664). On the other hand, the reflection peak at 2Θ = 33.3°, presented in the PS photoanode XRD spectrum, was attributed to (104) reflection. As reported in Table 1, the pulse discharge current during the PS deposition was 10-fold smaller than that for the HiPIMS mode. Thus, the energy of particles bombarding the substrate surface was lower in the former case but still much higher than expected in the MFS method. As a result, hematite adatoms tended to assemble in a different way, ultimately leading to the (104) texture. It is worth noting that, to the best of our knowledge, the majority of textured hematite films described in the literature were not obtained intentionally but most likely produced as a side effect of addition of metal dopants,[29−31] variation of the temperature,[32] and formation of 1D α-Fe_2O_3 nanoarchitectures.[33] The only direct approach leading to highly oriented hematite films along the (110) direction was proposed by Seki *et al.*[34] They used α-Al_2O_3(110) oriented substrates to epitaxially grow Rh doped hematite films by pulsed laser deposition method. However, the almost suppression of (104)

TABLE 1. Properties of Plasma Discharges during Deposition of the Hematite Photoanodes

sample acronym[a]	pulse discharge cathode current density j/[A/cm^2]	discharge pulsing frequency f_p/[kHz]	duty factor of pulsing cycle d_u/[%]	discharge current in pulse [A]
HIPIMS	3.2	0.1	1%	60
PS	0.32	1	10%	6
MFS	0.046	50	70%	0.9

[a] HiPIMS, high impulse power magnetron sputtering; PS, pulse sputtering; MFS, medium frequency sputtering.

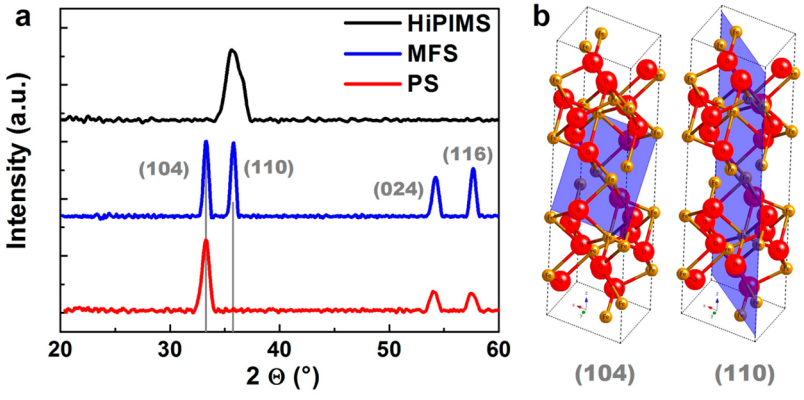

Figure 1. (a) X-ray diffraction patterns of hematite films deposited on the amorphous fused silica substrates; (b) models of the hematite crystal lattice with (104) and (110) preferentially oriented planes displayed.

alignment in favor of the (110) orientation and its impact on the hematite PEC activity has not previously been reported.

The hematite crystal structure of the films deposited on the FTO substrates was further verified using Raman spectroscopy. In Supporting Information Figure S3, all seven predicted Raman active phonon modes ($2A_{1g} + 5E_g$) of the hematite structure without any admixtures are clearly observed. The lowest A_{1g} mode at ~223 cm^{-1} exhibited largest intensity for HiPIMS samples, whereas the intensities of other modes are more comparable. This phenomenon can also be attributed to the (110) texture of the HiPIMS films. The obtained Raman data were analyzed similarly to the work by Munisso *et al.*[35] Preliminary simulations of the Raman response of A_{1g} and E_g modes in a crystal of D_{3d} symmetry in backscattering configuration seem to indicate that, for a broad choice of model parameters, the ratio between the averaged response of A_{1g} and E_g modes tends to be larger in case of prevailing (110) orientation of the surface than for other situations where the scattering vector is not perpendicular to the *c*-axis. This is particularly the case of the HiPIMS hematite films. More details about the model applied are given in Supporting Information.

Further evidence for strong preferential orientation of the crystallites was provided by ^{57}Fe conversion electron Mössbauer spectroscopy (CEMS).[36,37] CEMS spectra of the HiPIMS, MFS and PS samples are presented in Figure 2, which shows that all the spectra could be fitted with one magnetically split (sextet) component with hyperfine parameters typical for well crystalline hematite (Supporting Information Table S1). Considering the detection limit of Mössbauer spectroscopy (~3% of relative spectrum area), hematite was the only iron containing phase in all three analyzed samples. Preferential orientation of the magnetic moments (*i.e.*, texture effect) could be identified and quantified by evaluation of the relative intensities of the spectral lines. Generally, the intensities of spectral lines in a sextet are in the ratio of 3:*x*:1:1:*x*:3, where *x* varies from 0 to 4. The texture effect can be quantified through angle θ, which is defined as the average angle between the magnetic moments and direction of the γ-ray beam originating from the Mössbauer source. The angle θ can be determined directly by using the equation $x = [4(1 - \cos^2\theta)/(1 + \cos^2\theta)]$. In the absence of the texture effect ($x = 2$), the value of θ is ~55°. Smaller values of θ imply that magnetic moments are preferentially oriented along the γ-ray beam, which is perpendicular to the layer surface. In contrast, θ values larger than 55° indicate preferential orientation of the magnetic moments along the layer surface. The determined values of *x* and θ including errors are presented in Supporting Information Table S1. Clearly, the hematite film

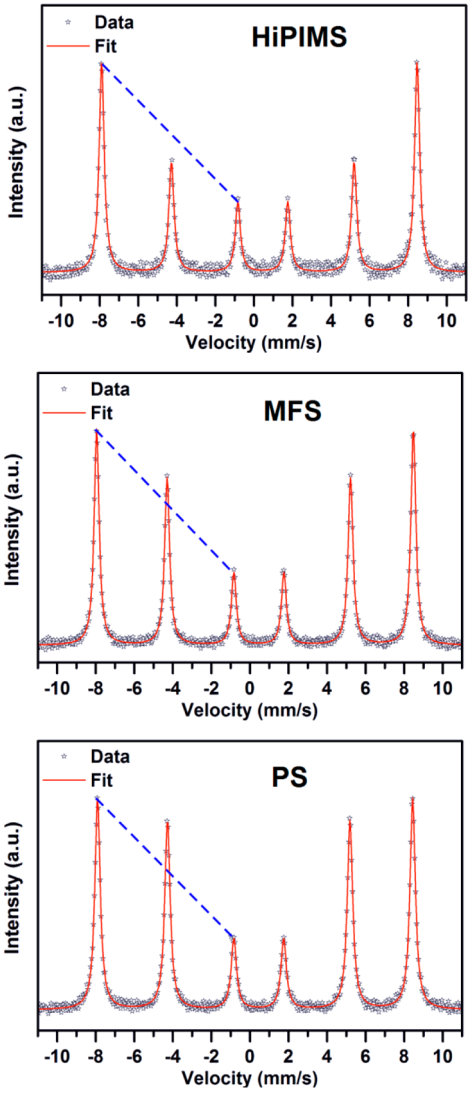

Figure 2. CEMS spectra of the hematite photoanode samples. The texture effect determined from the differences in relative intensity of the second spectral line.

prepared by the HiPIMS method exhibited preferential crystal orientation perpendicular to the substrate surface, as indicated by the θ value of 48.8 ± 1.4°, whereas the film prepared by the PS approach showed preferential growth along the surface, as reflected by the θ value of 63.7 ± 0.6°.

The surface morphology of the films was analyzed by atomic force microscopy (AFM) and the results are presented in Figure 3a and Supporting Information Figure S3. These figures also show scanning electron microscopy (SEM) cross-section images, which confirmed that all the films had a comparable thickness of 45 nm. This thickness was identified as optimal for the PEC water splitting activity in our previous study.[38] When the thickness was minimized, the negative effect of the short diffusion length of photogenerated holes was effectively suppressed.[38,39] The AFM surface image shown in Figure 3a suggests that the hematite crystallites in the HiPIMS film were predominantly aligned

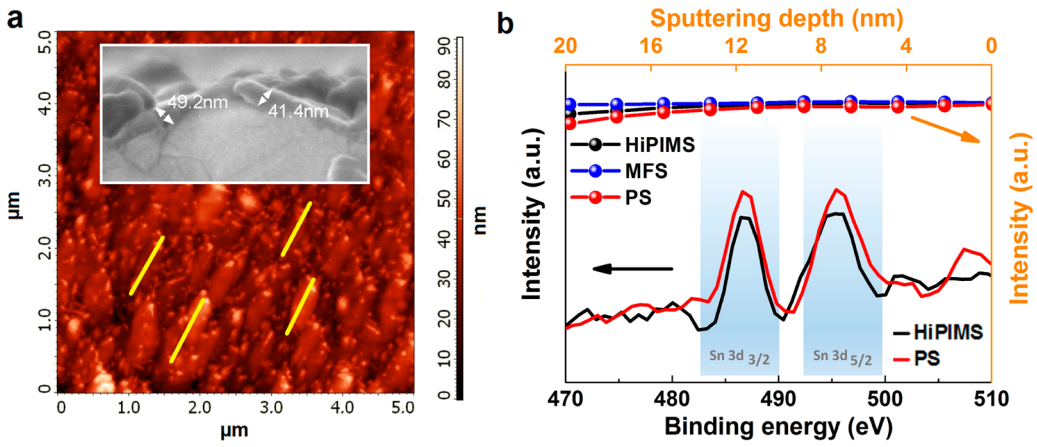

Figure 3. (a) AFM surface morphology image of HiPIMS fabricated photoanode. The yellow lines indicate the preferential orientation of crystallites. The inset shows the SEM cross-section image describing the thickness of the film to be around 45 nm; (b) the high resolution Sn 3d XPS spectra (bottom *x* and left *y* axis) with Sn depth profiling (up *x* and right *y* axis).

vertical to the substrate, which is another indication of their preferential orientation. In contrast, only randomly oriented grains in the MFS film were observed by AFM (Supporting Information Figure S5a). Although a slightly patterned surface can be distinguished in the AFM image of the PS film (Supporting Information Figure S5b), the preferential orientation detected by XRD was not as well reflected or recognizable as in the case of the HiPIMS film. The reason can be probably found in the preferential (104) orientation of the hematite grains, which is parallel toward the substrate.

To determine whether the observed properties and functionality were influenced by different concentrations of tin dopant serving as the carriers' donor, the elemental composition of the photoanodes was investigated by X-ray photoelectron spectroscopy (XPS). The high resolution XPS Sn 3d peaks intensities are presented in Figure 3b for the HiPIMS and PS films, since these two photonodes exhibited the biggest difference in water splitting activity (see discussion below), along with XPS Sn 3d depth profile curves for all three types of films. Two main peaks at 487.9 eV (Sn 3d3/2) and 496.3 eV (Sn 3d5/2) showing almost identical overall intensity were apparent in the spectra of the HiPIMS and PS films. In case of the MFS electrode, the Sn 3d peaks are seen in the full XPS survey and as a high resolution depth profile peaks (Sn 3d3/2 and Sn 3d5/2) evolution in Supporting Information Figure S6. The concentration XPS Sn 3d depth profiles for all three photoanodes (Figure 3b) were almost totally overlapped, suggesting their equivalent elemental composition. Moreover, almost equal full survey representative XPS spectra as same as the XPS O, Fe and Sn elemental depth profiles are seen in Supporting Information Figures S6a and S7, respectively. All these XPS analyses thus confirmed that the relatively low temperature of thermal annealing (650 °C), which is the main driving force for the Sn doping coming from

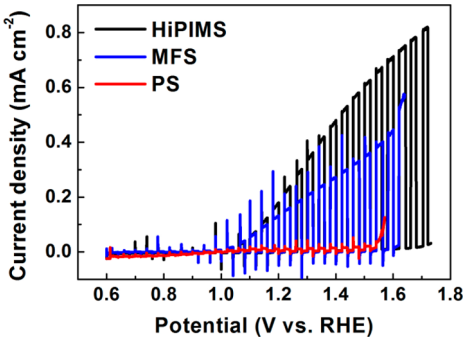

Figure 4. Simulated PEC water splitting activity of hematite photoanodes deposited under different energy of substrate ion bombardment. The PEC characteristics were recorded under solar light AM 1.5 simulated conditions with an intensity of 100 mW cm^{-2}, using 1 M KOH solution as the electrolyte, and with a scan rate of 1 mV s^{-1}.

the FTO substrate, did not caused any significant difference of the films composition among all three tested photoanodes.

Large differences in the PEC simulated water splitting performance were observed between the tested films (Figure 4). In these experiments, *J*−*V* polarization curves were measured under standard AM 1.5 G (intensity 100 mW cm^{-2}) chopped light illumination. The highest photocurrent values (0.28 mA cm^{-2} at 1.23 V and 0.65 mA cm^{-2} at 1.55 V *versus* RHE) were obtained with the HiPIMS fabricated hematite photoanodes. These values are among the highest PEC water splitting performances reported recently on bare (without any modifications) planar thin film hematite electrodes. A brief comparison is given in Table 2.[40−44] Since all experimental conditions were kept identical and the examined photoanodes differed principally in the preferential alignment of the crystallites, the excellent photoactivity of the HiPIMS photoanode was most likely due to the favorable conductivity of the majority carriers (electrons) along the [110] axis (*c*-axis) perpendicularly connected to the FTO substrate.

TABLE 2. Recently Reported PEC Water Splitting Current Density Values on Bare (without any Modifications) Hematite Planar Thin Film Photoanodes under 1.5 AM (100 mW cm^{-2}) Illumination in 1 M NaOH Electrolyte

reference	*J* at 1.23 V *vs* RHE [mA cm^{-2}]	*J* at 1.4 V *vs* RHE [mA cm^{-2}]
This work	0.28	0.5
40	0.11	0.2
41	0.18	0.6
42	0.05	0.1
43	0.18	0.4
44	0.10	0.3

We argue that a smaller size of the grains could only partially contribute to the enhanced photoactivity, as deduced from the XRD peak broadening seen in Figure 1. On the other hand, any noticeable difference of the XRD peak width corresponding to the PS and MFS electrodes was not revealed, while the difference in their PEC activity was significant. The second highly textured hematite photoanode deposited using the PS mode exhibited an almost negligible plateau photocurrent of 0.02 mA cm^{-2} at 1.23 V *versus* RHE, which remained almost constant until the water oxidation dark current onset. This drastic decrease can be explained by the synergetic effect of low electron and hole mobilities within the (104) plane oriented parallel to the *c*-axis and its nonideal oxygen dominated surface termination, which is believed to cause much higher surface recombination due to the high density of surface states acting as traps.[45] This issue was irrelevant for the (110) preferential orientation because its surface termination was dominated by Fe(III) ions. Moreover, this hypothesis was proved experimentally by measuring transient photocurrents, as discussed below. The most cathodically shifted dark current onset (Figure 4) corresponding to the PS photoanode can also be attributed to the surface or defect states. According to the work by Peter *et al.*,[46] these states can initiate water oxidation without illumination throughout the electron transfer that involves tunneling across the space-charge region. In between the two extremes (HiPIMS and PS films), the photoactivity of the untextured MFS films showed a photocurrent maxima of 0.14 mA cm^{-2} at 1.23 V and 0.38 mA cm^{-2} at 1.55 V *versus* RHE. This result is consistent with the XRD patterns, which showed that both discussed planes were present almost equally. Hence, the negative and positive roles of the preferential planes as well as surface terminations probably compensated each other, resulting in the average PEC performance.

Figure 5 shows a graph of the photocurrent maxima recorded at 1.55 V *versus* RHE plotted against the angle θ (from CEMS). The results clearly support the previous findings regarding the principal effect of crystal orientation on the PEC performance. Among

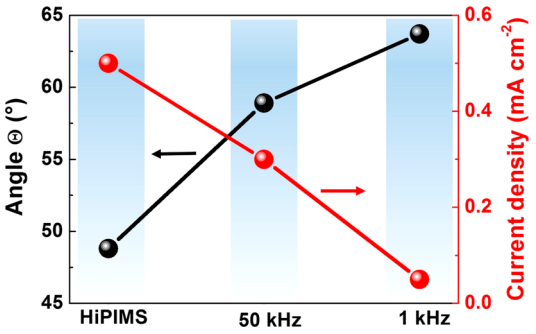

Figure 5. Correlation between the texture effect expressed as the angle Θ and the PEC activity of the films expressed as the photocurrent value read at 1.5 V *versus* RHE.

the prepared films, only the MFS method led to an untextured polycrystalline film composition, as confirmed by XRD, AFM, and CEMS techniques. The angle θ was determined to be 58.9 $\pm$ 0.4° for the MFS sample, which supports the aforementioned result. The lowest angle θ of 48.8 $\pm$ 1.4°, which can be attributed to the (110) preferential orientation, was obtained with the HiPIMS film. In contrast, the PS film showed the largest angle θ of 63.7 $\pm$ 0.6°, corresponding to the (104) preferential plane orientation. All the photoanodes showed highly consistent results from the methods employed for characterization, including XRD, Raman spectroscopy, CEMS, AFM, and PEC activity.

As stated above, the various preferential orientations of hematite crystallites also determine the organization of terminating atoms (Fe, O) at the surface. Figure 6a compares transient photocurrents under chopped monochromatic light (360 nm) illumination measured at an applied potential of 1.5 V *versus* RHE. The photocurrent transients exhibited negative and positive spike characteristics, suggesting strong surface recombination. On the basis of the previously proposed explanation, the anodic current spikes (positive current response) were attributed to accumulated holes at the photoelectrode/electrolyte interface, which were not injected into the electrolyte due to slow water oxidation kinetics. Instead, they are trapped by surface states. Conversely, the cathodic transient spikes (negative current response) were generated when the light was off, indicating back recombination of the accumulated (trapped) holes at the interface by electrons diffusing from the external circuit.[47] Oxygen vacancies have been proposed to act as electron traps and recombination centers.[48] If this is the case, the probability of defect states is expected to be much higher for a surface with a greater proportion of terminal oxygen ions. In agreement with theory,[40] the highest ratio between the steady state photocurrent and the transient photocurrent spike maximum demonstrating the lowest surface recombination was observed for the HiPIMS photoanode. For this photoanode, the extent of backward electron/hole

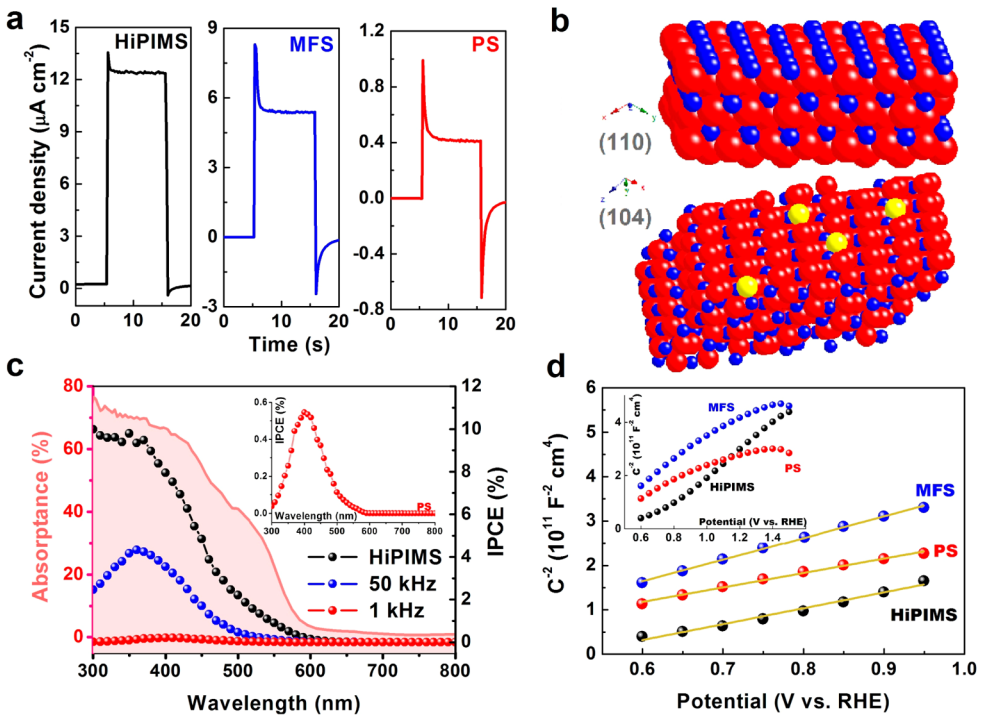

Figure 6. (a) Transient photocurrents initiated by the monochromatic (360 nm) light illumination and measured under an applied potential bias of 1.5 V; (b) models of hematite crystal lattices of (110) and (104) surface terminating planes; the blue, red, and yellow balls represent iron and oxygen atoms, and oxygen vacancies acting as the surface traps, respectively; (c) IPCE characteristics; (d) Mott−Schottky plots. All electrochemical experiments were done in 1 M KOH electrolyte.

recombination was reduced owing to the Fe(III) surface termination of the (110) plane and its substantially higher conductivity (Figure 6b). In contrast, this ratio was lowest for the (104) plane orientation displaying oxygen termination and the lowest conductivity among the examined films (Figure 6b). The assumption of the surface recombination due to oxygen vacancies was furthermore supported by measuring polarization curves in the electrolyte containing 0.5 M H_2O_2 introducing an easily oxidized hole scavenger that readily capture the photogenerated holes at the electrode/electrolyte interface. In this way the surface recombination is efficiently minimized. Current density plots as a function of applied potential are presented in Supporting Information Figure S8. Under dark conditions, the water oxidation dark current onsets showed the same trend (Supporting Information Figure S8a) as in the situation without presence of H_2O_2 in the electrolyte as it is seen in the Figure 4. When the electrodes absorbed light (Supporting Information Figure S8b), the photocurrent onsets were cathodically shifted in case of all three electrodes examined, which is, on the other hand, a common feature of the photoanodes, when a hole scavenger is applied.[47,48] Then, the photocurrents propagated over the entire potential range until the water oxidation dark current onset. A noteworthy increase of the photocurrent was observed for the PS films when compared to the photocurrent maxima reached in the bare NaOH electrolyte (see Figure 4). It indicated that the injection barrier (the recombination centers) for the holes was overcome. To the contrary, a much lower concentration of defect states was expected for the HiPIMS electrode having the iron dominated surface termination. As a consequence, indeed, the photocurrent maxima remained nominally the same apart from the aforementioned shift of the photocurrent onset.

Next, the incident photon to current efficiency (IPCE) was measured over the spectral range of 300−600 nm. The obtained IPCE data are plotted in Figure 6c together with the UV−vis absorption spectrum of the HiPIMS photoanode measured by photothermal deflection spectroscopy (PDS).[49] The basic optical properties of the HiPIMS and PS types of photoanodes were similar, as shown in Supporting Information Figure S9. The UV−vis absorption spectra in Figure 6c (filled area beneath the red absorption curve) qualitatively follow the detected IPCE behavior between 380 and 800 nm. As expected, the main trends of the IPCE curves were consistent with the AM 1.5 generated PEC polarization curves (see Figure 4). The highest IPCE value of 11% at around 350 nm was achieved with the HiPIMS photoanode. Considerably worse IPCE values of 4% and only 0.9% were obtained with the MFS and PS photoanodes, respectively. Hisatomi *et al.*[50] have attributed a similar decrease in IPCE to deteriorating charge transport. Thus, this may explain the results for our fabricated hematite coatings.

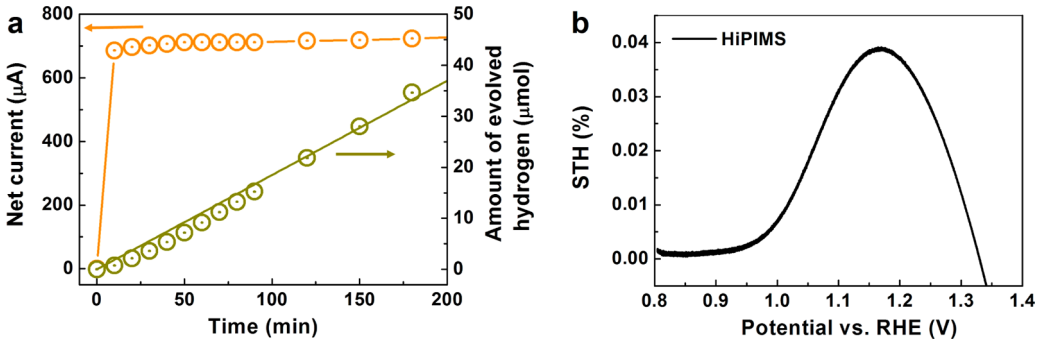

Figure 7. (a) Water splitting efficiency of the HiPIMS fabricated photoanode expressed as the amount of evolved hydrogen (green circles) and the long-term stability (orange circles). The measurements were performed by illuminating 2 cm^2 of the photoanode's area using AM 1.5 G light source of 100 mW/cm^2 intensity and with constant applied potential to the hematite photoanode of 1.5 V *versus* RHE. (b) Solar-to-hydrogen efficiency calculated according to eq 2.

To further elucidate the electronic properties of the photoanodes in contact with an electrolyte, electrochemical impedance measurements were performed. These nonilluminated measurements are typically presented as Mott–Schottky plots, which can be used to estimate the flat band potential (V_{Fb}) and apparent density of donors (N_D) of PEC photoelectrodes according to the Mott–Schottky equation.[51] The linear parts of the obtained Mott–Schottky plots are shown in Figure 6d. From the slopes of the linear extrapolations, the apparent donor densities were calculated as 4.92×10^{18}, 3.62×10^{18}, and 5.42×10^{18} cm^{-3}, for the HiPIMS, MFS, and PC films, respectively. These values are clearly very similar, despite the different plasma deposition modes used. This is an important result, which verifies that the superior photoefficiency is not caused or improved by a high density of majority carriers, and it furthermore supports the conclusions derived from the XPS examination. Moreover, over an extended applied potential region (0.4–1.6 V), the Mott–Schottky curves exhibited nonlinear behavior, as shown in the inset in Figure 6d. These nonideal characteristics have been directly linked to the presence of surface states in the work by Schrebler *et al.*[52] This further indicates that the surface states are due to the oxygen-rich surfaces, since the nonlinear trends of the Mott–Schottky curves were particularly pronounced for the MFS and PC hematite films (inset in Figure 6d).

The hydrogen evolution due to the solar-driven water splitting with the HiPIMS photoanode applied in the PEC system was measured by gas chromatography over a period of 200 min. The amount of photogenerated hydrogen gas as a function of operating time is presented in Figure 7a. The graph also contains the photocurrent values reached during the measurement under the applied voltage of 1.5 V *versus* RHE, which was kept constant. The graph denotes sufficiently long time stability of the HiPIMS electrode. The same electrodes have been repeatedly used during one year without any significant changes of their photoactivity. The Faradaic efficiency was estimated to be above 95%, which indicates that most of photogenerated charges were consumed by the PEC water splitting reactions. Figure 7b shows the solar-to-hydrogen efficiency (STH) as a function of applied potential until the 1.23 V *versus* RHE. The main issue causing the low observed STH is viewed in the high photocurrent onset potential, which can, on the other hand, still be shifted cathodically by several approaches.[9,53] In this way, the overall photoefficiency would be remarkably enhanced.

CONCLUSION

In summary, we have developed a powerful method for reproducibly generating hematite crystalline films highly oriented along the (110) plane. The hematite films were synthesized by a reactive magnetron sputtering technique utilizing deposition modes differing in the energy of ion flux. It was demonstrated that by careful selection of the deposition plasma parameters, the energy of heavy ions impinging on the surface of the substrate can be tuned to control the texture of the growing films. The highest energy bombarding particles were achieved with the HiPIMS technique, which generated hematite films with the desired crystalline alignment along the (110) direction. In contrast, the PS and MFS modes gave significantly lower energy and negligible bombardment, respectively. While the MFS mode showed no texture effect at all, the PS mode led to partial preferential orientation of the (104) plane. In agreement with the (110) texture conductivity prediction, the HiPIMS fabricated photoanodes demonstrated the highest PEC water splitting activity. In contrast, the hematite films showing preferential orientation along the (104) crystalline plane exhibited 10 times lower photocurrent maxima. The present results would induce further works enabling the controllable texture of hematite films and resulting in enhanced PEC performances. In this respect, HiPIMS technique is very promising approach, mainly if other parameters (*e.g.*, cation doping) will be involved and combined with the texture related phenomena. Described plasma deposition system is suitable for a combination of these highly active

textured hematite films with various so-called host-scaffold nanoarchitectures, which would induce further improvement of the overall photoefficiency by a substantial increase in the light harvesting.

METHODS

Fe_2O_3 thin films were deposited by DC pulse reactive magnetron sputtering of the cathode made of a pure iron target (99.95%) in a gas mixture of Ar + O_2. A circular balanced magnetron with a target diameter of 50 mm was used. The magnetron was placed in a high vacuum reactor chamber continuously pumped by turbomolecular and roughing pump. A substrate was placed in a distance of 50 mm from the surface of the iron target. For all the conditions presented in this work, the total gas pressure and partial pressures of argon and oxygen were held constant by controlling of their particular mass flow rate into the reactor chamber. The flow of argon was Q_{Ar} = 26 sccm and oxygen Q_{O2} = 20 sccm. The total pressure in the reactor was p = 1.2 Pa. Three different pulsing regimes of magnetron discharge operation were tested in this deposition experiment. For all experiments, the total average discharge current I_{AV}, and consequently the average current density j_{AV}, was held constant. The average current and current density were held on the value I_{AV} = 600 mA and j_{AV} = 32 mA/cm^2, respectively. The cathode pulse current density was the main parameter varied in this experiment. The change of pulse discharge current density, j_D, was provided by the change of pulsing frequency, f_P, together with the change of duty factor, d_u, of pulsing cycle. The films were deposited all with the same thickness of t_h = 45 nm in order to rule out influence of different thickness on structure, texture and other properties of hematite films. The films were deposited on glass substrate with SnO:F transparent conductive electrode (FTO, TCO-7, Solaronix), fused silica substrate, and multilayered substrate consisting of Pt/TiO_2/SiO_2/Si (Advanced Ceramic Coating Technology) with the hematite coating on the Pt side.

The crystalline phase of the Fe_2O_3 films was determined by X-ray powder diffraction (XRD) employing an X'Pert MRD powder diffractometer (parallel beam geometry realized with the Goebel mirror in the primary beam and parallel plate collimator and graphite monochromator in the secondary beam) and using Raman spectroscopy with a Renishaw Raman Microscope RM 1000 (unpolarized beam in back scattering mode of a 514.5 nm Ar^+ laser). Optical properties were investigated by means of photothermal deflection spectroscopy (PDS) based on the deviation of the laser beam collinearly propagated with the sample surface. The surface topography images were recorded by an Ntegra Aura. The cross-section images were obtained with help of a field emission scanning electron microscope (Hitachi FE-SEM S4800, Japan). Chemical characterization was carried out by X-ray photoelectron spectroscopy (PHI 5600, spectrometer) using Al Kα monochromatized radiation.

The samples of hematite thin films were characterized by ^{57}Fe conversion electron Mössbauer spectroscopy (CEMS) employing a CEMS2010 spectrometer. The CEMS spectrometer is equipped with a proportional continuous gas flow counter filled with a Penning mixture consisting of 90% He and 10% CH_4. A 50 mCi ^{57}Co(Rh) Mössbauer γ-ray source (14.41 keV) was used inside the spectrometer. Unfolded spectra were registered at room temperature to 1024 channels for 3−5 days and then fitted by the MossWinn 4.0 software package. The CEMS method enables to selectively characterize iron containing phases (including amorphous or nanocrystalline) within the depth of layers up to 300 nm. Moreover, a texture effect (*i.e.*, a preferential orientation of magnetic moments) can be observed and quantified through the relative intensity of the second spectral line of a sextet component.

The photoelectrochemical experiments were carried out under simulated AM 1.5 (100 mW cm^{-2}) illumination provided by a solar simulator (300 W Xe with optical filter, Solarlight; room temperature) in 1 M KOH solution. A three-electrode configuration was used in the measurements, with the iron oxide electrode as the working electrode (photoanode), an Ag/AgCl (3 M KCl) as the reference electrode, and a platinum foil as the counter electrode. Photocurrent *versus* voltage (I−V) characteristics were recorded by scanning the potential from OCP to 0.4 V (*versus* Ag/AgCl) with a scan rate of 1 mV s^{-1} using a Jaissle IMP 88 PC potentiostat.

Photocurrent spectra were acquired at an applied potential of 0.5 V (*versus* Ag/AgCl) in 1 M KOH recorded with 10 nm steps in the range of 300−700 nm using an Oriel 6365 150 W Xe-lamp equipped with a Oriel Cornerstone 7400 1/8 m monochromator. Incident photocurrent conversion efficiencies (IPCE) were calculated by IPCE = $(1240 i_{ph})/(\lambda I_{light})$, where i_{ph} is the photocurrent density (mA cm^{-2}), λ is the incident light wavelength (nm), and I_{light} (mW cm^{-2}) is the intensity of light source at each wavelength. The Mott−Schottky curves were acquired with a Zahner IM6 potentiostat (Zahner Elektrik, Kronach, Germany). Measurements were obtained under dark conditions at a frequency of 500 Hz in 1 M KOH solution. A three-electrode configuration was used in the measurements, where the α-Fe_2O_3 electrode served as the working electrode (photoanode), a saturated Ag/AgCl as the reference electrode and a platinum foil as the counter electrode.

The measured potentials *versus* Ag/AgCl were converted to the reversible hydrogen electrode (RHE) scale following the Nernst equation:

$$E_{RHE} = E_{Ag/AgCl} + 0.059\ pH + E^{o}_{Ag/AgCl} \quad (1)$$

where E_{RHE} is the converted potential *versus* RHE, $E^{o}_{Ag/AgCl}$ = 0.1976 at 25 °C, and $E_{Ag/AgCl}$ is the experimentally measured potential against the Ag/AgCl reference.

The time stability of the hematite photoanodes and the concentration of produced hydrogen were tested by the following setup. Two chamber glass cell with 1 M NaOH water solution working as the electrolyte was used. Anode and cathode chambers were separated by the glass frit to prevent mixing of the electrolyte. Potential of +1.5 V *versus* RHE was applied to the sample (working electrode). Platinum sheet was used as the counter electrode. Each chamber was bubbled by argon gas (1 mL/min) separately. The illuminated area of the photoanode was 2 cm^2. The chambers were open to air by glass capillary to avoid mixing with air. Output gas from cathode chamber (platinum counter electrode) was analyzed by gas chromatograph (Master, Dani) equipped with plot column (Rt-Msieve 5A, Restek) and mTCD detector (Vici).

The solar-to-hydrogen efficiency η_{STH} was calculated according to the eq 2:

$$\eta_{STH(\%)} = J_p[(1.23 - V_{app})/I_0] \quad (2)$$

where J_p is the photocurrent density (in mA/cm^2), I_0 is the intensity of incident light (in mW/cm^2), and V_{app} is the applied potential to the photoanode in (V *versus* RHE).

Conflict of Interest: The authors declare no competing financial interest.

Supporting Information Available: Schematic arrangement of HiPIMS deposition system, extended X-ray diffraction spectra, Raman spectra, model polarized Raman spectra, additional AFM and SEM images, XPS full survey spectra, current density *versus* applied potential curves, optical properties, values of Mössbauer hyperfine parameters, and recently reported PEC water splitting current density values. The Supporting Information is available free of charge on the ACS Publications website at DOI: 10.1021/acsnano.5b01740.

Acknowledgment. The authors acknowledge support from the Ministry of Education, Youth and Sports of the Czech Republic (LO1305), the Grant Agency of the Czech Republic (project 13-29241P) and from the Ministry of Education, Youth and Sports of the Czech Republic (project LH12043).

REFERENCES AND NOTES

1. Chu, S.; Majumdar, A. Opportunities and Challenges for a Sustainable Energy Future. *Nature* **2012**, *488*, 294–303.
2. Walter, M. G.; Warren, E. L.; McKone, J. R.; Boettcher, S. W.; Mi, Q.; Santori, E. A.; Lewis, N. S. Solar Water Splitting Cells. *Chem. Rev.* **2010**, *110*, 6446–6473.
3. Gratzel, M. Photoelectrochemical Cells. *Nature* **2001**, *404*, 338–344.
4. Sivula, K.; Le Formal, F.; Grätzel, M. Solar Water Splitting: Progress Using Hematite (α-Fe_2O_3) Photoelectrodes. *ChemSusChem* **2011**, *4*, 432–449.
5. Murphy, A. B.; Barnes, P. R. F.; Randeniya, L. K.; Plumb, I. C.; Grey, I. E.; Horne, M. D.; Glasscock, J. A. Efficiency of Solar Water Splitting Using Semiconductor Electrodes. *Int. J. Hydrogen Energy* **2006**, *31*, 1999–2017.
6. Kim, J. Y.; Magesh, G.; Youn, D. H.; Jang, J.-W.; Kubota, J.; Domen, K.; Lee, J. S. Single-Crystalline, Wormlike Hematite Photoanodes for Efficient Solar Water Splitting. *Sci. Rep.* **2013**, *3*, 2681.
7. Brillet, J.; Yum, J. H.; Cornuz, M.; Hisatomi, T.; Solarska, R.; Augustynski, J.; Grätzel, M.; Sivula, K. Highly Efficient Water Splitting by a Dual-Absorber Tandem cell. *Nat. Photonics* **2012**, *6*, 823–827.
8. Liu, R.; Zheng, Z.; Spurgeon, J.; Yang, X. Enhanced Photoelectrochemical Water-Splitting Performance of Semiconductors by Surface Passivation layers. *Energy Environ. Sci.* **2014**, *7*, 2504–2517.
9. Kment, S.; Hubicka, Z.; Krysa, J.; Sekora, D.; Zlamal, M.; Olejnicek, J.; Cada, M.; Ksirova, P.; Remes, Z.; Schmuki, P.; et al. On the Improvement of PEC Activity of Hematite Thin Films Deposited by High-Power Pulsed Magnetron Sputtering Method. *Appl. Catal., B* **2015**, *165*, 344–350.
10. Ling, Y.; Wang, G.; Wheeler, D. A.; Zhang, J. Z.; Li, Y. Sn-Doped Hematite Nanostructures for Photoelectrochemical Water Splitting. *Nano Lett.* **2011**, *11*, 2119–2125.
11. Morin, F. J. Electrical Properties of α-Fe_2O_3 and α-Fe_2O_3 Containing Titanium. *Phys. Rev.* **1951**, *83*, 1005–1010.
12. Morin, F. J. Electrical Properties of α-Fe_2O_3. *Phys. Rev.* **1954**, *93*, 1195–1199.
13. Rosso, K. M.; Smith, D. M. A.; Dupuis, M. An *ab Initio* Model of Electron Transport in Hematite (α-Fe_2O_3) Basal Planes. *J. Chem. Phys.* **2003**, *118*, 6455–6466.
14. Iordanova, N.; Dupuis, M.; Rosso, K. M. Charge Transport in Metal Oxides: A Theoretical Study of Hematite α-Fe_2O_3. *J. Chem. Phys.* **2005**, *122*, 144305.
15. Liao, P.; Toroker, M. C.; Carter, E. A. Electron Transport in Pure and Doped Hematite. *Nano Lett.* **2011**, *11*, 1775–1781.
16. Bosman, A. J.; Vandaal, H. J. Small Polaron *versus* Band Conduction in Some Transition Metal Oxides. *Adv. Phys.* **1970**, *19*, 1–117.
17. Goodenough, J. B. Metallic Oxides. *Prog. Solid State Chem.* **1971**, *5*, 145–399.
18. Nakau, T. Electrical Conductivity of α-Fe_2O_3. *J. Phys. Soc. Jpn.* **1960**, *15*, 727.
19. Cornuz, M.; Grätzel, M.; Sivula, K. Preferential Orientation in Hematite Films for Solar Hydrogen Production *via* Water Splitting. *Chem. Vap. Depos.* **2010**, *16*, 291–295.
20. Helmersson, U.; Lattemann, M.; Bolmark, J.; Ehiasarian, A. P.; Gudmundsson, J. T. Ionized Physical Vapor Deposition (IPVD): A Review of Technology and Applications. *Thin Solid Films* **2006**, *513*, 1–24.
21. Fujimura, N.; Nishihara, T.; Goto, S.; Xu, J. F.; Ito, T. Control of Preferred Orientation for ZnO_x Films—Control of Self-Texture. *J. Cryst. Growth* **1993**, *130*, 269–279.
22. Wan, D. Y.; Huang, F. Q.; Wang, Y. M.; Mou, X. L.; Xu, F. F. Highly Surface-Textured ZnO:Al Films Fabricated by Controlling the Nucleation and Growth Separately for Solar Cell Applications. *ACS Appl. Mater. Interfaces* **2010**, *2*, 2147–2152.
23. Ehiasarian, A. P.; Vetushka, A.; Gonzalvo, Y. A.; Safran, G.; Szekely, L.; Barna, P. B. Influence of High Power Impulse Magnetron Sputtering Plasma Ionization on the Microstructure of TiN Thin Films. *J. Appl. Phys.* **2011**, *109*, 104314.
24. Sarakinos, K.; Alami, J.; Konstantinidis, S. High Power Pulsed Magnetron Sputtering: A Review on Scientific and Engineering State of the Art. *Surf. Coat. Technol.* **2010**, *204*, 1661–1684.
25. Samuelsson, M.; Lundin, D.; Jensen, J.; Raadu, M. A.; Gudmundsson, J. T.; Helmersson, U. On the Film Density Using High Power Impulse Magnetron Sputtering. *Surf. Coat. Technol.* **2010**, *205*, 591–596.
26. Patsalas, P.; Gravalidis, S.; Logothetidis, S. Surface Kinetics and Subplantation Phenomena Affecting the Texture, Morphology, Stress, and Growth Evolution of Titanium Nitride Films. *J. Appl. Phys.* **2004**, *96*, 6234–6246.
27. Agura, H.; Suzuki, A.; Matsushita, T.; Aoki, T.; Okuda, M. Low Resistivity Transparent Conducting Al-Doped ZnO Films Prepared by Pulsed Laser Deposition. *Thin Solid Films* **2003**, *445*, 263–267.
28. Bohlmark, J.; Lattemann, M.; Gudmundsson, J. T.; Ehiasarian, A. P.; Gonzalvo, Y. A.; Brenning, N.; Helmersson, U. The Ion Energy Distributions and Ion Flux Composition from a High Power Impulse Magnetron Sputtering Discharge. *Thin Solid Films* **2006**, *515*, 1522–1526.
29. Kay, A.; Cesar, I.; Grätzel, M. New Benchmark for Water Photooxidation by Nanostructured α-Fe_2O_3 films. *J. Am. Chem. Soc.* **2006**, *128*, 15719–15721.
30. Zhang, X.; Li, H.; Wang, S.; Fan, F. F.; Bard, J. A. Improvement of Hematite as Photocatalyst by Doping with Tantalum. *J. Phys. Chem. C* **2014**, *118*, 16842–16850.
31. Liu, J.; Cai, Y. Y.; Tian, Z. F.; Ruan, G. S.; Ye, Y. X.; Liang, C. H.; Shao, G. S. Highly Oriented Ge-Doped Hematite Nanosheet Arrays for Photoelectrochemical Water Oxidation. *Nano Energy* **2014**, *9*, 282–290.
32. Bora, D. K.; Braun, A.; Erat, S.; Safonova, O.; Graule, T.; Constable, E. C. Evolution of Structural Properties of Iron Oxide Nano Particles during Temperature Treatment from 250 °C-900 °C: X-ray Diffraction and Fe K-Shell Pre-Edge X-ray Absorption Study. *Curr. Appl. Phys.* **2012**, *12*, 817–825.
33. Wang, L.; Lee, C.-Y.; Schmuki, P. Solar Water Splitting: Preserving the Beneficial Small Feature Size in Porous α-Fe_2O_3 Photoelectrodes during Annealing. *J. Mater. Chem. A* **2013**, *1*, 212–215.
34. Seki, M.; Yamahara, H.; Tabata, H. Enhanced Photocurrent in Rh-Substituted α-Fe_2O_3 Thin Films Grown by Pulsed Laser Deposition. *Appl. Phys. Express* **2012**, *5*, 115801.
35. Munisso, M. C.; Zhu, W.; Pezzotti, G. Raman Tensor Analysis of Sapphire Single Crystal and Its Application to Define Crystallographic Orientation in Polycrystalline Alumina. *Phys. Status Solidi B* **2009**, *246*, 1893–1900.
36. Cesar, I.; Sivula, K.; Kay, A.; Zboril, R.; Grätzel, M. Influence of Feature Size, Film Thickness, and Silicon Doping on the Performance of Nanostructured Hematite Photoanodes for Solar Water Splitting. *J. Phys. Chem. C* **2009**, *113*, 772–782.
37. Frydrych, J.; Machala, L.; Tucek, J.; Siskova, K.; Filip, J.; Pechousek, J.; Safarova, K.; Vondracek, M.; Seo, J. H.; Schneeweiss, O.; et al. Facile Fabrication of Tin-Doped Hematite Photoelectrodes—Effect of Doping on Magnetic Properties and Performance for Light-Induced Water Splitting. *J. Mater. Chem.* **2012**, *22*, 23232–23239.
38. Kment, S.; Hubicka, Z.; Krysa, J.; Olejnicek, J.; Cada, M.; Gregora, I.; Zlamal, M.; Brunclikova, M.; Remes, Z.; Liu, N.; et al. High-Power Pulsed Plasma Deposition of Hematite Photoanode for PEC Water Splitting. *Catal. Today* **2014**, *230*, 8–14.
39. Le Formal, F.; Gratzel, M.; Sivula, K. Controlling Photoactivity in Ultrathin Hematite Films for Solar Water-Splitting. *Adv. Funct. Mater.* **2010**, *20*, 1099–1107.
40. Zhang, Y.; Jiang, S.; Song, W.; Zhou, P.; Ji, H.; Ma, W.; Hao, W.; Chen, Ch.; Zhao, J. Nonmetal P-doped Hematite Photoanode with Enhanced Electron Mobility and High Water Oxidation Activity. *Energy Environ. Sci.* **2015**, *8*, 1231–1236.
41. Steier, L.; Herraiz-Cardona, I.; Gimenez, S.; Fabregat-Santiago, F.; Bisquert, J.; Tilley, S. D.; Gratzel, M. Understanding the Role of Underlayers and Overlayers in Thin Film Hematite Photoanodes. *Adv. Funct. Mater.* **2014**, *24*, 7681–7688.

42. Kim, D. W.; Riha, S. C.; DeMarco, E. J.; Martinson, A. B. F.; Farha, O. K.; Hupp, J. T. Green Lighting Photo Electrochemical Oxidation of Water by Iron Oxide. *ACS Nano* **2014**, *8*, 12199–12207.
43. Young, K. M. H.; Hamann, T. W. Enhanced Photocatalytic Water Oxidation Efficiency with $Ni(OH)_2$ Catalysts Deposited on α-Fe_2O_3 *via* ALD. *Chem. Commun.* **2014**, *50*, 8727.
44. Zandi, O.; Beardslee, J. A.; Hamann, T. Substrate Dependent Water Splitting with Ultrathin α-Fe_2O_3 Electrodes. *J. Phys. Chem. C* **2014**, *118*, 16494–16503.
45. Kilner, J.; Skinner, S.; Irvine, S.; Edwards, P. *Functional Materials for Sustainable Energy Applications*; Wooddhead Publishing Ltd.: New York, NY, 2012.
46. Peter, L. M.; Wijayantha, K. G. U. Photoelectrochemical Water Splitting at Semiconductor Electrodes: Fundamental Problems and New Perspectives. *ChemPhysChem* **2014**, *15*, 1983–1995.
47. Dotan, H.; Sivula, K.; Gratzel, M.; Rothschild, A.; Warren, S. C. Probing the Photoelectrochemical Properties of Hematite (α-Fe_2O_3) Electrodes Using Hydrogen Peroxide as a Hole Scavenger. *Energy Environ. Sci.* **2011**, *4*, 958–964.
48. Sivula, K. Metal Oxide Photoelectrodes for Solar Fuel Production, Surface Traps, and Catalysis. *J. Phys. Chem. Lett.* **2013**, *4*, 1624–1633.
49. Kment, S.; Kluson, P.; Hubicka, Z.; Krysa, J.; Cada, M.; Gregora, I.; Deyneka, A.; Zabova, H.; Jastrabik, L. Double Hollow Cathode Plasma Jet-Low Temperature Method for the $TiO_{2-x}N_x$ Photoresponding Films. *Electrochim. Acta* **2010**, *55*, 1548–1556.
50. Hisatomi, T.; Dotan, H.; Stefik, M.; Sivula, K.; Rothschild, A.; Gratzel, M.; Mathews, N. Enhancement in the Performance of Ultrathin Hematite Photoanode for Water Splitting by an Oxide Underlayer. *Adv. Mater.* **2012**, *24*, 2699–2702.
51. Klahr, B. M.; Martinson, A. B. F.; Hamann, T. W. Photoelectrochemical Investigation of Ultrathin Film Iron Oxide Solar Cells Prepared by Atomic Layer Deposition. *Langmuir* **2011**, *27*, 461–468.
52. Schrebler, R.; Ballesteros, L. A.; Gomez, H.; Grez, P.; Cordova, R.; Munoz, E.; Schrebler, R.; Ramos-Barrado, J. R.; Dalchiele, A. Electrochemically Grown Self-Organized Hematite Nanotube Arrays for Photoelectrochemical Water Splitting. *J. Electrochem. Soc.* **2014**, *161*, H903–H908.
53. Zandi, O.; Hamann, T. W. Enhanced Water Splitting Efficiency Through Selective Surface State Removal. *J. Phys. Chem. Lett.* **2014**, *5*, 1522–1526.